# Theoretical Investigation of Transport Across Superconductor/Ferromagnetic Interfaces

by

Dheepak Surya Kalyana Raman

A Thesis Presented in Partial Fulfillment
of the Requirements for the Degree
Master of Science

Approved November 2018 by the
Graduate Supervisory Committee:

Nathan Newman, Chair
Christopher Muhich
David. K. Ferry

ARIZONA STATE UNIVERSITY

December 2018

ABSTRACT

Attaining a sufficiently large critical current density ($J_c$) in magnetic-barrier Josephson junctions has been one of the greatest challenges to the development of dense low-power superconductor memories. Many experimentalists have used various combinations of superconductor (S) and ferromagnetic (F) materials, with limited success towards the goal of attaining a useful Jc. This trial-and-error process is expensive and time consuming. An improvement in the fundamental understanding of transport through the ferromagnetic layers and across the superconductor-ferromagnetic interface could potentially give fast, accurate predictions of the transport properties in devices and help guide the experimental studies.

In this thesis, parameters calculated using density functional methods are used to model transport across Nb/0.8 nm Fe/Nb/Nb and Nb/3.8 nm Ni /Nb/Nb Josephson junctions. The model simulates the following transport processes using realistic parameters from density functional theory within the generalized gradient approximation: (a) For the first electron of the Cooper pair in the superconductor to cross the interface- conservation of energy and crystal momentum parallel to the interface ($k_{ll}$). (b) For the second electron to be transmitted coherently- satisfying the Andreev reflection interfacial boundary conditions and crossing within a coherence time, (c) For transmission of the coherent pair through the ferromagnetic layer- the influence of the exchange field on the electrons' wavefunction and (d) For transport through the bulk and across the interfaces- the role of pair-breaking from spin-flip scattering of the electrons. Our model shows the utility of using realistic electronic-structure band properties of the materials used, rather

the mean-field exchange energy and empirical bulk and interfacial material parameters used by earlier workers. [Kontos *et al*. Phys. Rev Lett, *93*(13), 137001. (2004); Demler *et al*. Phys. Rev. B, 55(22), 15174. (1997)].

The critical current densities obtained from out model for Nb/0.8 nm Fe/Nb is $10^4$ A/cm$^2$ and for Nb/3.8 nm Ni/Nb is $7.1*10^4$ A/cm$^2$. These values fall very close to those observed experimentally- i.e. for Nb/0.8 nm Fe/Nb is $8*10^3$ A/cm$^2$ [Robinson *et al*" Phys. Rev. B 76, no. 9, 094522. (2007)] and for Nb/3.8 nm of Ni/Nb is $3*10^4$ A/cm$^2$ [Blum *et al* Physical review letters 89, no. 18, 187004. (2002). This indicates that our approach could potentially be useful in optimizing the properties of ferromagnetic-barrier structures for use in low-energy superconducting memories.

# ACKNOWLEDGMENTS

I would first like to thank my research advisor Dr. Nathan Newman for his valuable guidance, consistent encouragement, personal caring and timely help. The state of the art facilities at Newman Research group and his helpful insights made this work possible.

I am thankful to Dr. Christopher Muhich for his constant support and sharing his invaluable knowledge density functional theory, the software and many more things related to theoretical investigation of materials. I would also like to thank Dr. David. K. Ferry, for his constant support and advice on density functional and band theory.

I would like to thank Ms. Archana Ramanathan Seshakrishnan for her invaluable contribution in python, and helping me build various scripts for data analysis.

I would like to acknowledge Mr. Justin Gonzales from my group for his invaluable time and support for helping me a lot with theoretical simulations and density functional calculations. I would like to acknowledge all members of Dr. Christopher Muhich's group, namely Ms. Srashtasrita Das, for helping me a lot in VASP and in density functional in relation to the simulations run for this thesis

I extend my thanks to Mr. Richard Hanley for having assisted me in solving numerous facility problems in the lab. I want to thank Mr. Cameron Kopas, Mr. Siddhesh Gajare, Mr. Madhu Krishna Murthy, Mr. Ashwin Agathya Boochakravarthy, Mr. Kaiwen Zhang, Ms. Gayatri Pode and other members of the group for enlightening discussions and tremendous support.

I express my earnest thanks and deep sense of appreciation to my parents, family and friends for their timely advice and incomparable support.

TABLE OF CONTENTS Page

LIST OF TABLES

Table Page

LIST OF FIGURES

Figure Page

# CHAPTER 1 MOTIVATION AND INTRODUCTION

## 1.1 Introduction to JMRAM

A relatively recent proposal to create a low-power cryogenic memory is called JMRAM (Josephson magnetic random access memory). The devices are Josephson junctions which contain ferromagnetic barrier layers. Device operation uses the principle that the wavefunction of the coherent pairs rotates as they are transported through the ferromagnetic material. Two ferromagnetic layers are used in the most commonly used rendition of the JMRAM (Figure 1) so that (a) the wavefunction rotates by less than $\pi/2$ in the anti-parallel state, resulting in a conventional "0" junction and (b) by more than $\pi/2$ and less than $3\pi/2$ in the parallel state, resulting in a $\pi$-junction. [1] When this structure is used with a second conventional Josephson junction in parallel, as in a SQUID (superconductor quantum interference device) configuration, the JMRAM device can produce different transfer characteristics at zero-applied field, depending on whether the ferromagnetic layer in the junction is in a 0 (i.e. maximum Jc) or $\pi$-state (i.e. minimum Jc). [2] The Josephson implementation has all of the advantages of the conventional MRAM (magnetic random access memory): high speed, non-volatility with high write-erase endurance, and high storage density [3] [4]. JMRAM also has superconducting wiring that allows non-dissipative propagation of the signals with speed-of-light access time even in large memory arrays. [5]

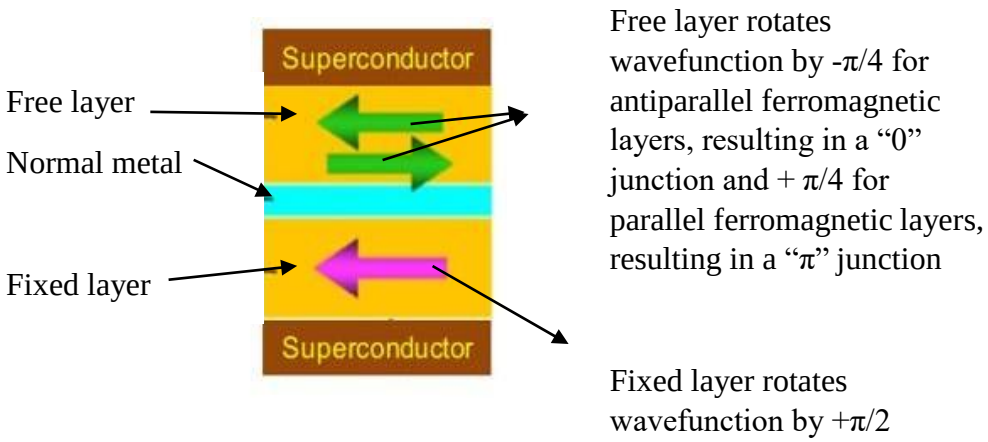


Figure 1: Illustration of one rendition of operation of a JMRAM device that can be programmed to be a "0" or "π" junction [6]

The fabrication of JMRAM devices have been realized [7]. However, in all of the devices, the critical current is found to be much smaller than predicted by the simplistic models that use the mean-field exchange energy and empirical bulk and interfacial material parameters [8]. In this thesis, we use realistic parameters from band theory to model transport across the interface and through the bulk to see if we can better understand the mechanism(s) that determine the critical current through the device.

**1.2 Density Functional Theory**:

Nuclei, with their much larger masses, move much slower than the electrons. The Born-Oppenheimer approximation assumes that one can consider the electrons moving in the field of the fixed nuclei. Thus, the electronic Hamiltonian reduces to

$$\hat{H}_{elec} = -\frac{1}{2}\sum_{i=1}^{N}\nabla_i^2 - \sum_{i=1}^{N}\sum_{A=1}^{M}\frac{Z_A}{r_{iA}} + \sum_{i=1}^{N}\sum_{j>i}^{N}\frac{1}{r_{ij}} = \hat{T} + \hat{V}_{Ne} + \hat{V}_{ee}$$

Figure 1: Hamiltonian for Density functional Theory [9]

The solution of the Schrodinger equation with $H_{elec}$ is the electronic wave function $\Psi_{elec}$ and the electronic energy $E_{elec}$. The total energy $E_{tot}$ is then the sum of $E_{elec}$ and the constant nuclear repulsion term $E_{nuc}$. [9]

$$\hat{H}_{elec}\Psi_{elec} = E_{elec}\Psi_{elec}$$

$$E_{tot} = E_{elec} + E_{nuc} \qquad \text{where} \quad E_{nuc} = \sum_{A=1}^{M}\sum_{B>A}^{M}\frac{Z_A Z_B}{R_{AB}}$$

Figure 2: Solution for density functional Hamiltonian [9]

### 1.2.1 Generalized Gradient Approximation

The first logical step to go beyond LDA is the use of not only the information about the density ρ ($\vec{r}$) at a particular point $\vec{r}$, but to supplement the density with information about the gradient of the charge density, ∇ρ ($\vec{r}$) in order to account for the non-homogeneity of the true electron density. Thus, we write the exchange-correlation energy in the following form termed generalized gradient approximation (GGA), [9]

$$E_{xc}[\rho\alpha, \rho\beta] = \int f(\rho\alpha, \rho\beta, \nabla\rho\alpha, \nabla\rho\beta)\, d\vec{r}$$

- GGA's and hybrid approximations has reduced the LDA errors of atomization energies of standard set of small molecules by a factor 3-5. This improved accuracy has made DFT a significant component of quantum chemistry. [9]
- All the present functionals are inadequate for situations where the density is not a slowly varying function. Examples are (a) Wigner crystals; (b) Van der Waals energies between non overlapping subsystems; (c) electronic tails evanescing into the vacuum near the surfaces of bounded electronic systems. However, this does not preclude that DFT with appropriate approximations can successfully deal with such problems. [9]

## CHAPTER 2 THE MODEL

In order to determine the critical current loss across the S/F interface, a model was designed that took into consideration a set of conditions that a pair of electron must satisfy to propagate across the interface and travel through the bulk of the ferromagnetic material coherently. [10] In our work the materials are assumed to be in the clean limit, indicating that the superconductor coherence and ferromagnet proximity length is larger than the mean free path and relative device dimensions. It is also assumed that the effect of perpendicular crystal momentum is negligible in affecting the critical current density of the device. The influence of defects in the bulk materials and at the interfaces are also neglected.

We assume that the superconductor is Nb with a critical current of $2 \times 10^7$ A/cm$^2$ up to the interface. [11]

For the conditions to cross the interface, we show below a simplified schematic of the Andreev conditions. To illustrate this in the simplest way, we use spherical Fermi surfaces and a single mean-field exchange energy.

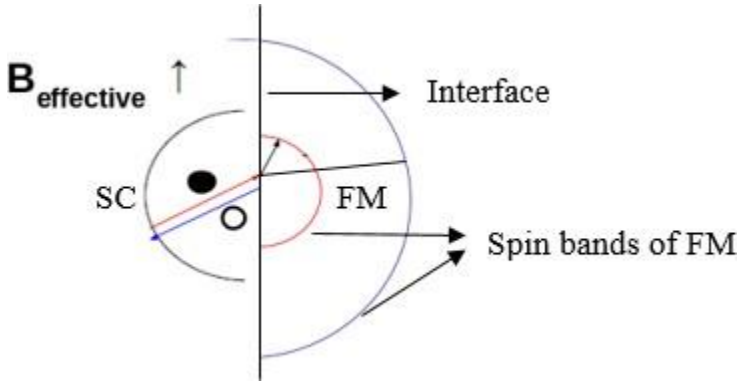


Figure 3: Andreev Reflection for free electron Fermi surfaces

This process involves three steps. For a pair of electrons to cross the S/F interface coherently, the following conditions must occur [12]:

1. The first electron conserves parallel crystal momentum and spin when crossing the interface. In our analysis, all equal $k_{\|}$-values on the superconductor Nb's Fermi surface directed towards the interface and on the ferromagnet's Fermi surfaces directed from the interface are identified, i.e.

   $k_{\|}$ (superconductor) = $k_{\|}$ (ferromagnet)..... 2.1

2. Then, the second electron must cross the interface within a coherence time while satisfying Andreev reflection conditions of conservation of momentum and energy across the interface. In the above diagram, twice the energy due to the Fermi surface on the left should be equal to the sum of the Fermi energies on the right.

   $2k_{\|}$ (superconductor) - $k_{spinup}$ (ferromagnet)-$k_{spindown}$ (ferromagnet) <= $k_{\|}$

(phonon) ..... 2.2

2E (superconductor) - $E_{spinup}$ (ferromagnet)-$E_{spindown}$ (ferromagnet) <=hν (phonon) .....2.3

In our analysis, we use these equations to identify all points in k-space that satisfy 2.1, 2.2 and 2.3. We also assume that all electrons cross within this coherence time.

3. We also consider the pair-breaking process of spin-flip scattering at the interface, which can be calculated using the following expression with the experimentally-determined parameters reported in Reference 13.

$P = [1 - \exp(-\delta)]$, where δ is the spin-flip parameter for interfaces and P is the probability of electrons that get spin flipped at the interface. [13]

The k-space vectors that satisfy these interfacial transport conditions within an energy window of +-50 meV, the energy of an optical phonon, are expected to be the dominant conduction channels across the interface are often referred to as "hot-spots".

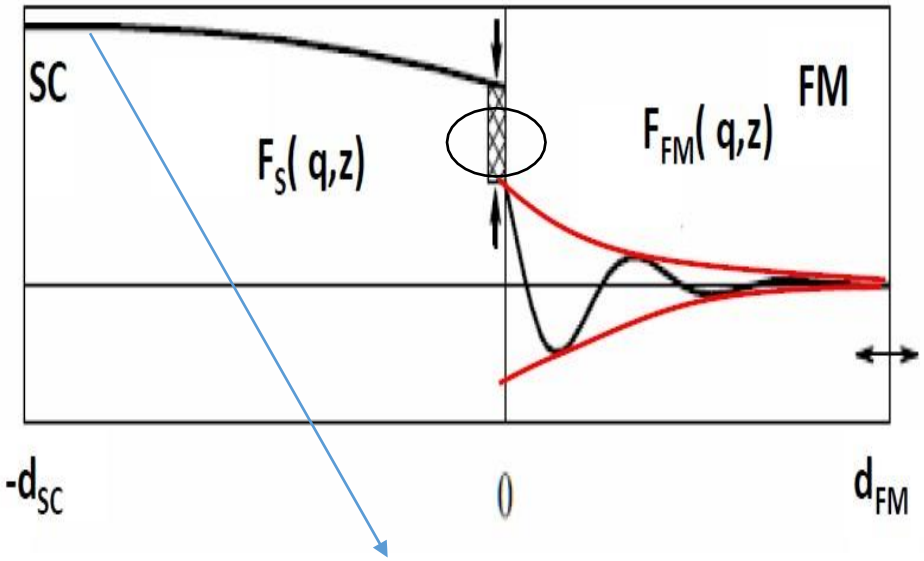


$J_C=2*10^7 A/cm^2$ [10]

Figure 4: Indication of dropping of wavefunction at the interface in a S/F pair [12]

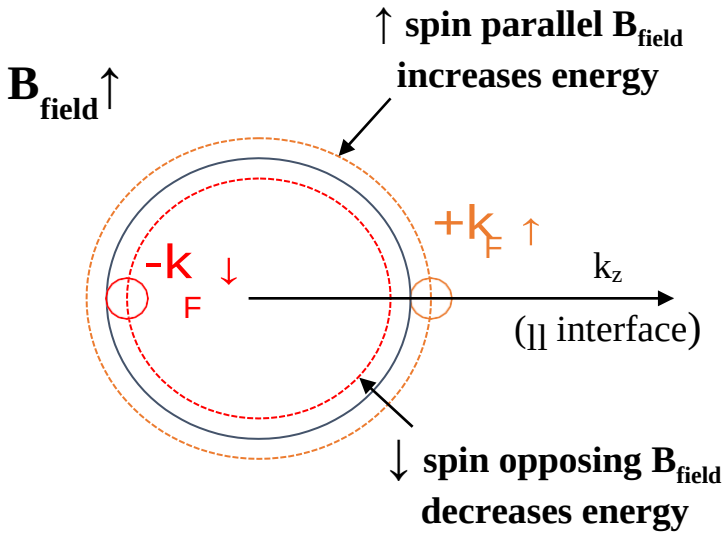


Figure 6: Description of pair transport across the S/F interface [12]

To model the transport of a coherent pair through the bulk ferromagnet, we note that the +k electron in the Cooper pair with spin in the direction of the field gains kinetic energy, while the -k electron loses kinetic energy, as predicted by the Stoner model (Figure 7). This results in the pair gaining a net momentum, $2E_x/v_F$, so the wavefunction is expected to both decay and oscillate according to

$$\psi = \psi_o e^{-2\pi T/ v_F} e^{i2(Ex)x/v_F} \text{ [12]} \quad \text{.....2.4}$$

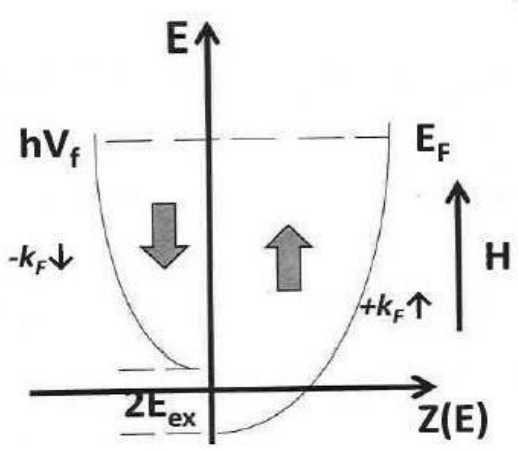


Figure 7: Stoner model for exchange field in ferromagnets [9] [12]

The real part of the equation corresponds to the rotation of the wavefunction during transport, and the imaginary part corresponds to the exchange splitting field that occurs due to the formation of the finite net momentum. The rotation part of the wavefunction leads to 1 since the wavefunction corresponds to a cosine wave, and cos π equals to -1. π

radians is taken to be the angle since we obtain the first maximum $J_c$ when the device is at $\pi$ rotation.

The decay in magnitude of the wavefunction, and thus the number of coherent pairs, is the result of the magnetic field causing the spins to align, thus breaking the spin up-spin down (↑↓) pairs of electrons.

As illustrated in Figure 8, the characteristic exchange splitting is k-dependent. From this, we see that the use of an average exchange energy would not be expected to result in an accurate prediction. Instead, the k-dependent exchange energy for each of the electrons that made it through the interface (i.e. at the hotspots) needs to be used.

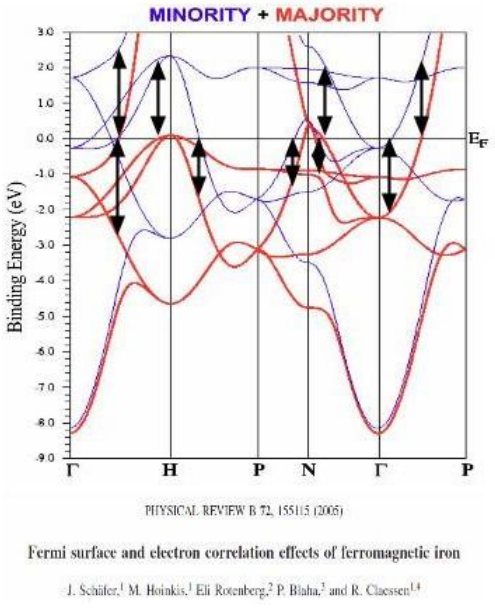


Figure 8: Example of majority minority band Exchange splitting in ferromagnetic iron [14]

Spin-flip scattering can also destroy coherent pairs. The rate of scattering is quantified with the spin diffusion length:

$L = \lambda_{sf} = (6*l_{sf}^2)/((1-\beta^2)*\lambda_t)$ [13] ..... 2.5

where L is the spin flip mean free path of the ferromagnetic material, β is the spin scattering asymmetry, $l_{sf}$ is the spin diffusion length and $\lambda_t$ is the transport mean free path. $\lambda_t$ can be calculated using the following expression.

$\lambda_t = [(R_q)(3\pi)/2k_F^2]/\rho$ [13] ..... 2.6

where $R_q$ is the quantum of resistance, 26 kΩ, $k_F$ is the wave-vector and ρ is the resistivity of niobium.

The probability of scattering is $P = [1 - \exp(-\delta)]$, where δ is the spin-flip interface parameter.

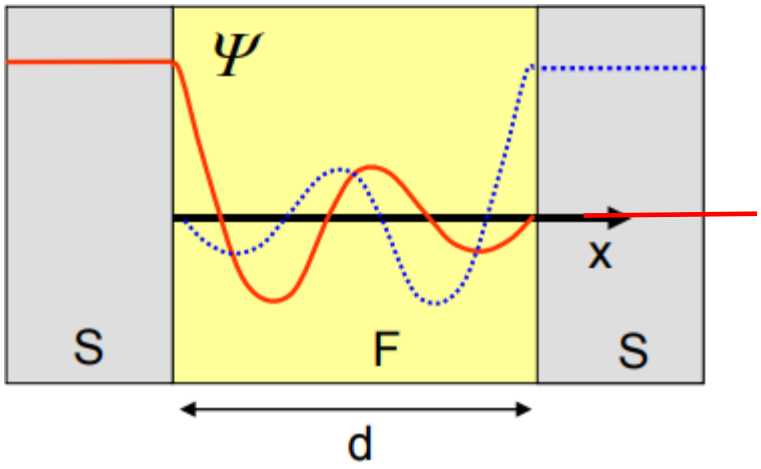


Figure 9: SFS wavefunction [12]

# CHAPTER 3 SOFTWARE

## 3.1 Vienna ab initio simulation package (VASP)

This section is adapted from reference [15], which is the VASP manual.

The software used to carry out the theoretical simulations is the Vienna Ab initio Simulation Package, also known as VASP

VASP, is a package for performing ab initio quantum mechanical molecular dynamics using either Vanderbilt pseudopotentials, or the projector augmented wave method, and a plane wave basis set. The basic methodology is density functional theory (DFT), but the code also allows use of post-DFT corrections such as hybrid functionals mixing DFT and Hartree–Fock exchange, many-body perturbation theory (the GW method) and dynamical electronic correlations within the random phase approximation.

VASP contains certain input files that is required to be fed in, for it to run a simulation. These input files are INCAR, POSCAR, POTCAR and KPOINTS. All these files have information or set of commands that the user needs to be prepare before running a simulation.

### 3.1.1 INCAR

The INCAR file is the central input file of VASP. It determines "what to do and how to do it". There is a relatively large number of parameters that may be set by means of tags in the INCAR file. Most of these parameters have convenient defaults, and a user unaware of their meaning should not change any of the default values.

```
System = NbFe
ALGO = FAST
LREAL = AUTO
NWRITE = 2
ENCUT = 400
EDIFF = 1E-5
EDIFFG = -1E-3
NELM = 100
NPAR = 28

ISMEAR = 1
SIGMA = 0.01

LVHAR = FALSE
LVTOT = TRUE
ISPIN = 2
ISIF = 3
ICHARGE = 2
LORBIT = 11
IBRION = 1
NSW = 40

PREC = ACCURATE
NUPDOWN = 12
MAGMOM = 4*0 6*3 4*0
```

Figure 10: Example INCAR file

### 3.1.2 Tags under INCAR:

ENCUT:

ENCUT specifies the cutoff energy for the plane-wave basis set in eV.

EDIFF:

EDIFF specifies the global break condition for the electronic self-consistency loop. The relaxation of the electronic degrees of freedom will be stopped if the total (free)

energy change and the band structure energy change ('change of eigenvalues') between two steps are both smaller than EDIFF.

EDIFFG:

EDIFFG defines the break condition for the ionic relaxation loop. If the change in the total (free) energy is smaller than EDIFFG between two ionic steps relaxation will be stopped.

NELM:

NELM sets the maximum number of electronic self-consistency steps which may be performed for the energy to converge.

NPAR:

NPAR defines the number of cores in which a simulation job should be carried out in parallel.

ISMEAR:

ISMEAR determines how the partial occupancies are set for each orbital.

- ISMEAR=0: Gaussian smearing.
- ISMEAR=−1: Fermi smearing.
- ISMEAR=−2: partial occupancies are read in from the WAVECAR or INCAR file, and kept fixed throughout run.

- ISMEAR=−3: perform a loop over smearing-parameters supplied in the INCAR file
- ISMEAR=−4: tetrahedron method
- ISMEAR=−5: tetrahedron method with Blöchl corrections

SIGMA:

SIGMA specifies the width of the smearing in eV

LVHAR and LVTOT:

Tags are used to generate the average potential of the input structure. LVHAR determines whether the total local potential includes the fields from all particles (ionic + Hartree + exchange-correlation) or just the electrostatic fraction (ionic + hartree). FALSE gives entire potential while TRUE gives electrostatic potential. LVTOT determines whether the potential is written into the LOCPOT file or not

ISPIN:

ISPIN specifies spin polarization

- ISPIN=1: non spin polarized calculations are performed.
- ISPIN=2: spin polarized calculations (collinear) are performed.

ISIF:

ISIF determines whether the stress tensor is calculated and which principal degrees-of-freedom are allowed to change in relaxation. ISIF determines whether the stress tensor is calculated. The calculation of the stress tensor is relatively time-consuming, and therefore by default switched off. In addition ISIF determines which degrees-of-freedom (ionic positions, cell volume, and cell shape) are allowed to change. The following table provides details on the tag

| ISIF | Calculate | | Degrees of Freedom | | |
|---|---|---|---|---|---|
| | forces | Stress tensor | positions | Cell shape | Cell volume |
| 0 | Yes | No | Yes | No | No |
| 1 | Yes | Trace only | Yes | No | No |
| 2 | Yes | Yes | Yes | No | No |
| 3 | Yes | Yes | Yes | Yes | Yes |
| 4 | Yes | Yes | Yes | Yes | No |
| 5 | Yes | Yes | No | Yes | No |
| 6 | Yes | Yes | No | Yes | Yes |
| 7 | Yes | Yes | No | No | Yes |

Table 3.1 List of options for using the ISIF tag

LORBIT:

LORBIT determines whether the PROCAR or PROOUT files are written. If the value of LORBIT is >10, there is no need to mention the Wigner-Seitz radius for each atom. LORBIT =11 generates a DOSCAR, which contains the data for density of states and a PROCAR file, which contains information on contribution of the s,p,d and f bands to the density of states with respect to each k-point in the mesh. This will also lead to an lm-decomposed PROCAR, which is useful in looking at individual band contributions through a space vector or a given plane.

### 3.1.3 POSCAR

This file contains the lattice geometry and the ionic positions. The first line is treated as a comment line (you should write down the name of the system). The second line provides a universal scaling factor (lattice constant), which is used to scale all lattice vectors and all atomic coordinates (of this value is negative it is interpreted as the total volume of the cell). On the following three lines the three lattice vectors defining the unit cell of the system are given (first line corresponding to the first lattice vector, second to the second, and third to the third). The sixth line supplies the number of atoms per atomic species (one number for each atomic species). The following lines gives us either the direct or Cartesian co-ordinates depending on what we feed into the system.

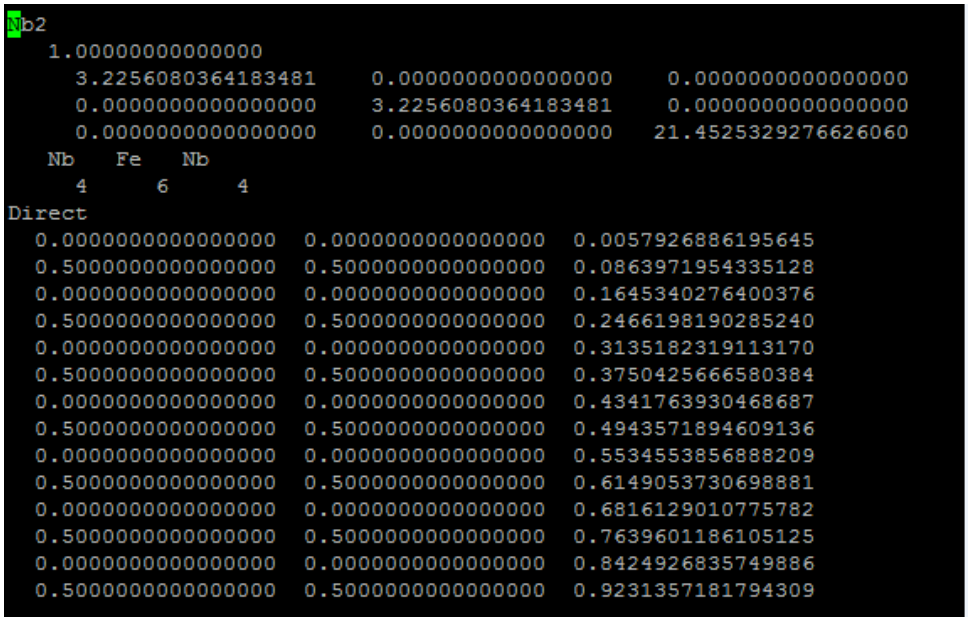


Figure 11: Example POSCAR file

### 3.1.4 POTCAR

The POTCAR file contains the pseudopotential for each atomic species used in the calculation. If the number of species is larger than one simply concatenates the POTCAR files of the species. On a UNIX machine you might type the line

cat ~/pbe/Nb_pv/POTCAR ~/pbe/Fe/POTCAR ~/pbe/Nb_pv/POTCAR > POTCAR

to generate POTCAR files for the aforementioned structure. The order in the POTCAR file should match the INCAR and POSCAR file fed into the system respectively.

### 3.1.5 KPOINTS

The file KPOINTS must contain the k-point coordinates and weights or the mesh size for creating the k-point grid.

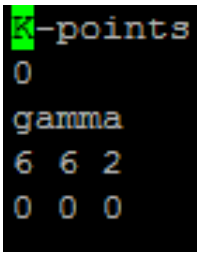


Figure 12: Example KPOINTS file

### 3.1.6 Output tags

DOSCAR:

The DOSCAR file contains the DOS and integrated DOS. The units are number of states/eV and number of states, respectively and thus extensively defined. The intensive DOS is obtained by dividing by the Volume of the unit cell.

OUTCAR:

The OUTCAR file gives detailed output of a VASP run, including: a summary of the used input parameters, information about the electronic steps, KS-eigenvalues, stress tensors, forces on the atoms, local charges and magnetic moments

PROCAR:

For static calculations, the file PROCAR contains the spd- and site projected wave function character of each band. It also specifies the contribution each and every band makes based on the k-point mesh to the whole band structure and the density of states

CHGCAR:

This file contains the lattice vectors, atomic coordinates, the total charge density

multiplied by the volume. It gives information on the charge density distribution across the stack of atoms that are simulated.

### 3.2 VESTA

A cross-platform program, VESTA, has been developed to visualize both structural and volumetric data in multiple windows with tabs. VESTA represents crystal structures by ball-and-stick, space-filling, polyhedral, wireframe, stick, dot-surface and thermal-ellipsoid models. A variety of crystal-chemical information is extractable from fractional coordinates, occupancies and oxidation states of sites. [16]

Volumetric data such as electron and nuclear densities, Patterson functions, and wavefunctions are displayed as isosurfaces, bird's-eye views and two-dimensional maps. Isosurfaces can be colored according to other physical quantities. Translucent isosurfaces and/or slices can be overlapped with a structural model. Electron densities determined experimentally are convertible into their Laplacians and electronic energy densities. [16]

Below is an example of a niobium bcc unit cell in VESTA.

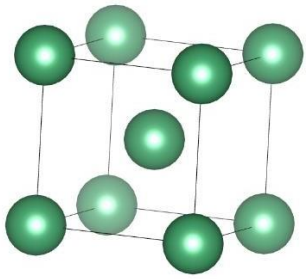

Figure 13: Unit cell of bcc Nb in VESTA

# CHAPTER 4 RESULTS AND DISCUSSION

## 4.1 Initial steps

A 14 atom elemental structure was created using the VESTA software. The unit cells for the materials niobium, nickel and iron are downloaded from a website called materials project [17]. The website contains all structural information pertaining to all the elements. Once the unit cells are downloaded, the positions of the atoms according to its structure, the POSCAR file information can be viewed using VESTA. By changing the unit cell parameters, one can create the required structure for the analyses required. The restructured POSCAR is saved and used for simulations in VASP.

The POSCAR file created before is copied into the system in VASP. The INCAR and POTCAR files are created as mentioned above. A mesh of 75*75*75 is created in the KPOINTS file. The job is run for every element separately. Our calculations used only bulk material electronic-structure parameters to model interfacial and bulk transport.

A series of steps are followed to determine the critical current density of the superconductor/ferromagnet/superconductor structure.

A huge set of k-space vectors are generated for niobium, iron and nickel are filtered on the basis of Fermi energies obtained in the system i.e. only the k-points whose energy is within $\pm$0.01 eV of the Fermi energy of the element. These calculations and further data analysis are carried out through the usage of python scripts.

```
i=0
header = ""
#5.6311
with open("../../Femesh/EIGENVAL") as fp, open("datasample.txt","w") as f:
    for line in fp:
        i=i+1
        if i>7:
            numbers = line.split()
            if len(numbers) == 4:
                header = line
            elif len(numbers) == 5:
                #data
                num1 = float(numbers[1])
                num2 = float(numbers[2])
                if num1 >= 5.6211 and num1 <= 5.6411:
                    if header != "":
                        f.write(header)
                        header = ""
                    f.write(line)
                elif num2 >= 5.6211 and num2 <= 5.6411:
                    if header != "":
                        f.write(header)
                        header = ""
                    f.write(line)
```

Figure 14: Python script for filtering near Fermi vectors for all the elements

In the above script, the k-points are accessed through the EIGENVAL file generated during a simulation. Then the energy of each k-point is compared to ±-0.01 eV of the Fermi energy, and if it falls under the range, the k-point along with its majority and minority splitting energies are printed in the output file.

Once the output file is obtained, the following steps are applied to the list of the k-points, one by one, which leads to the reduction of the number of k-points compared to the initial number. This set is then stored and used for calculation of critical current densities.

### 4.2 Transport in the superconductor

A critical current density of $2*10^7$ A/cm$^2$ is characteristic of a niobium superconductor. [11]

### 4.3 S/F Interface

a) Conservation of $k_{ll}$ and spin for the first electron of the Cooper pair crossing the interface

There are around 12000 wave-vectors found near the Fermi level of niobium. Once the filtering is completed, a list of all of the k-space points with equal k|| and that fall within the energy window of 50 meV for niobium and the ferromagnet are determined (i.e. equation 2.1). This results in a:

- reduction in $J_c$ by a factor of ~ 1/17 for iron. Thus, the critical current is reduced at the interface by the momentum conditions alone to ~ $J_{c\ (Fe)}$ ~ $1.2*10^6$ A/cm$^2$.
- reduction in $J_c$ by a factor of ~ 1/9 for nickel. Thus, the critical current is reduced at the interface by the momentum conditions alone to $2.2*10^6$ A/cm$^2$.

Andreev reflection condition: conservation of energy and momentum across the interface when the second electron crosses the interface within a coherence time of $2\Delta/\hbar$ =0.235 ps. The list of k-points that satisfied the momentum conservation conditions within the energy window for Nb/0.8 nm Fe/Nb and Nb/3.8 nm Ni /Nb are then accessed to see if they also satisfy the

requirements imposed by Andreev reflection using a similar python script to above using the following conditions. Then computed for critical current densities and the following values are obtained from equations 2.2 and 2.3. The conduction through a given hotspot is proportional to the density of states and thus the number of k-points satisfying the interface conditions in the specified energy window.

The fractional reduction in $J_c$ is ~1/16 for iron-barrier junctions, reducing the critical current density to - $J_{c\ (Fe)} \sim 7.5*10^4$ A/cm$^2$. The fractional reduction in $J_c$ is ~1/11 for nickel-barrier junctions, reducing the critical current density to $J_{c\ (Ni)} \sim 2*10^5$ A/cm$^2$.

An illustration of hotspots in k-space are illustrated below. Each point has a symmetric 2, 4 or 8 points, depending on their coordinates.

| S no | Nb vectors satisfying (a) and (b) near the Fermi level | | | Fe vectors satisfying (a) and (b) near the Fermi level | | |
|---|---|---|---|---|---|---|
| | $K_x$ | $K_y$ | $K_z$ | $K_x$ | $K_y$ | $K_z$ |
| 1 | 0.44 | 0.12 | 0 | 0.44 | 0.12 | 0 |
| 2 | 0.346 | 0.253 | 0 | 0.346 | 0.253 | 0.16 |
| 3 | 0.346 | 0.253 | 0.013 | 0.346 | 0.253 | 0.16 |
| 4 | 0.44 | 0.12 | 0.093 | 0.44 | 0.12 | 0 |
| 5 | 0.36 | 0.2 | 0.093 | 0.36 | 0.2 | 0.146 |
| 6 | 0.493 | 0.28 | 0.12 | 0.493 | 0.28 | 0.053 |
| 7 | 0.293 | 0.186 | 0.133 | 0.293 | 0.186 | 0.08 |
| 8 | 0.453 | 0.386 | 0.253 | 0.453 | 0.386 | 0.026 |

Table 4.1 List of Fermi vectors of Niobium and Iron that satisfies equations 2.1, 2.2 and 2.3

| S no | Nb vectors satisfying (a) and (b) near the Fermi level | | | Ni vectors satisfying (a) and (b) near the Fermi level | | |
|---|---|---|---|---|---|---|
| | kx | ky | kz | kx | ky | Kz |
| 1 | 0.48 | 0.28 | 0 | 0.48 | 0.28 | 0.08 |
| 2 | 0.48 | 0.28 | 0.013333 | 0.48 | 0.28 | 0.08 |
| 3 | 0.48 | 0.266667 | 0.026667 | 0.48 | 0.266667 | 0.026667 |
| 4 | 0.48 | 0.28 | 0.026667 | 0.48 | 0.28 | 0.08 |
| 5 | 0.12 | 0.12 | 0.04 | 0.12 | 0.12 | 0.053333 |
| 6 | 0.48 | 0.266667 | 0.04 | 0.48 | 0.266667 | 0.026667 |
| 7 | 0.48 | 0.28 | 0.04 | 0.48 | 0.28 | 0.08 |
| 8 | 0.133333 | 0.106667 | 0.053333 | 0.133333 | 0.106667 | 0.053333 |
| 9 | 0.12 | 0.12 | 0.053333 | 0.12 | 0.12 | 0.053333 |
| 10 | 0.386667 | 0.213333 | 0.053333 | 0.386667 | 0.213333 | 0.106667 |
| 11 | 0.48 | 0.266667 | 0.053333 | 0.48 | 0.266667 | 0.026667 |
| 12 | 0.48 | 0.28 | 0.053333 | 0.48 | 0.28 | 0.08 |
| 13 | 0.133333 | 0.106667 | 0.066667 | 0.133333 | 0.106667 | 0.053333 |
| 14 | 0.12 | 0.12 | 0.066667 | 0.12 | 0.12 | 0.053333 |
| 15 | 0.48 | 0.266667 | 0.066667 | 0.48 | 0.266667 | 0.026667 |
| 16 | 0.28 | 0.28 | 0.066667 | 0.28 | 0.28 | 0.053333 |
| 17 | 0.426667 | 0.266667 | 0.08 | 0.426667 | 0.266667 | 0 |
| 18 | 0.48 | 0.28 | 0.08 | 0.48 | 0.28 | 0.08 |
| 19 | 0.12 | 0.106667 | 0.093333 | 0.12 | 0.106667 | 0 |
| 20 | 0.48 | 0.28 | 0.093333 | 0.48 | 0.28 | 0.08 |
| 21 | 0.453333 | 0.28 | 0.12 | 0.453333 | 0.28 | 0.08 |
| 22 | 0.453333 | 0.293333 | 0.146667 | 0.453333 | 0.293333 | 0.08 |
| 23 | 0.466667 | 0.306667 | 0.173333 | 0.466667 | 0.306667 | 0.066667 |
| 24 | 0.453333 | 0.346667 | 0.213333 | 0.453333 | 0.346667 | 0.173333 |
| 25 | 0.48 | 0.36 | 0.253333 | 0.48 | 0.36 | 0.053333 |
| 26 | 0.466667 | 0.373333 | 0.266667 | 0.466667 | 0.373333 | 0.04 |
| 27 | 0.426667 | 0.426667 | 0.266667 | 0.426667 | 0.426667 | 0.133333 |
| 28 | 0.453333 | 0.44 | 0.306667 | 0.453333 | 0.44 | 0.24 |
| 29 | 0.48 | 0.48 | 0.32 | 0.48 | 0.48 | 0.266667 |
| 30 | 0.493333 | 0.493333 | 0.32 | 0.493333 | 0.493333 | 0.28 |

Table 4.2 List of Fermi vectors of Niobium and Nickel that satisfies equations 2.1, 2.2 and 2.3

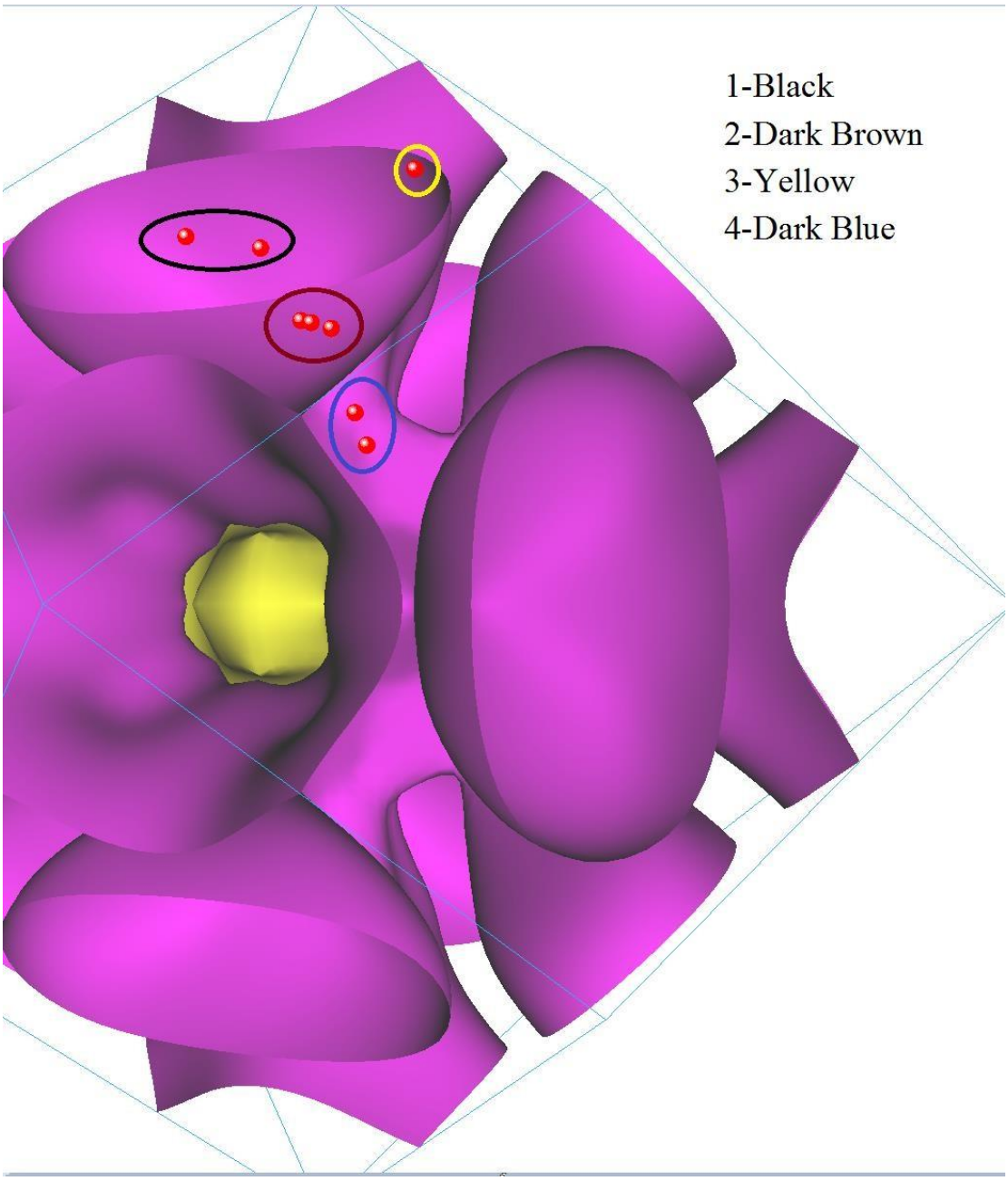


Figure 15: Fermi surface of niobium with iron hot spots

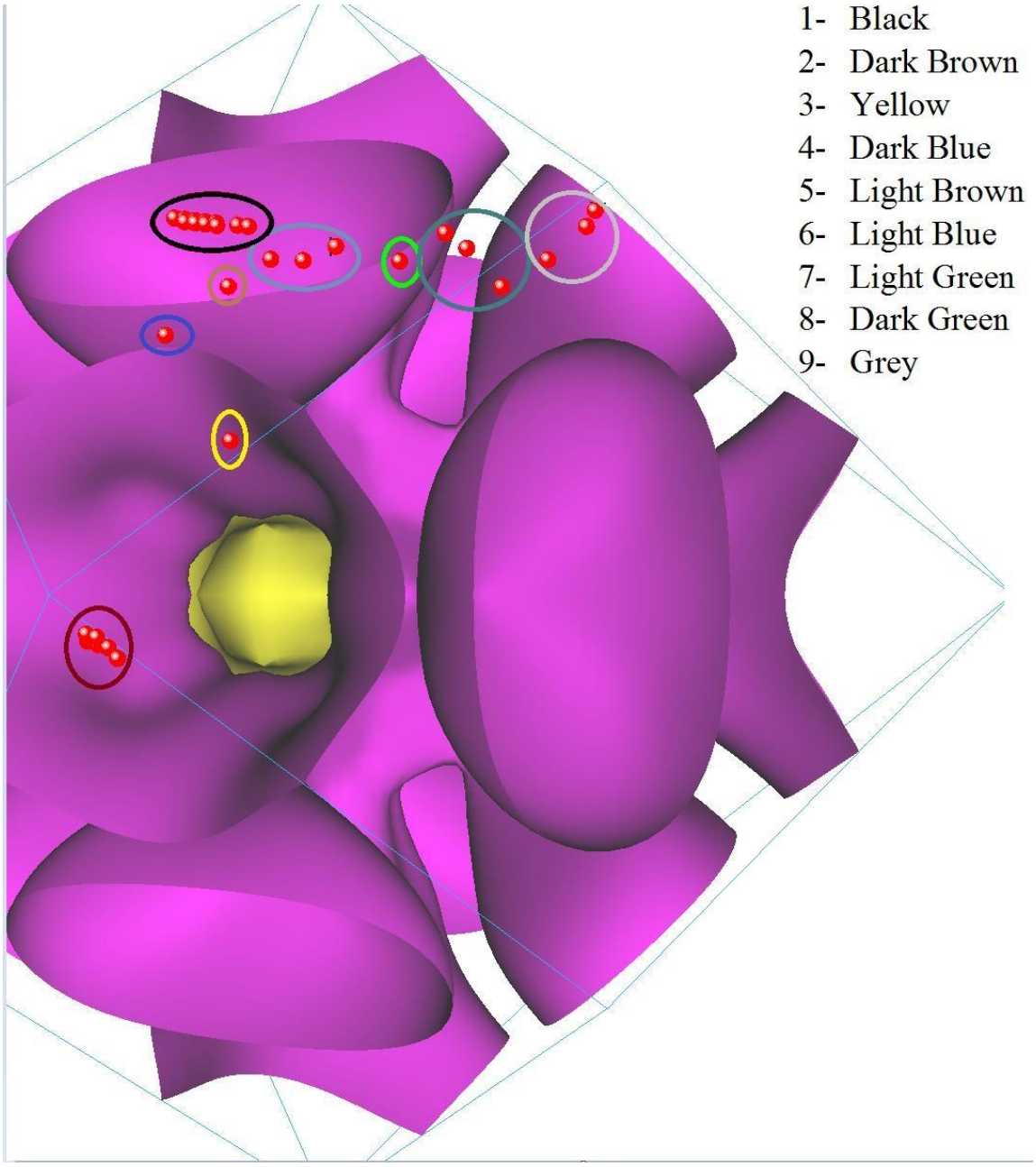

Figure 56: Fermi surface of niobium with nickel hot spots

b) Spin-flip scattering at the interface

The spin-flip parameter [13] is a parameter at S/N and S/F interfaces that depends on the amount of accumulation resistance an interface has. Accumulation resistance is defined as the resistance due to the accumulation of minority spin electrons at the interface, that causes extra resistance for the pairs during transport, and hence leading to pair-breaking [13][18]. Thus, a fraction of the electrons transmitted across the interface undergo a spin-flip process. This can be quantified using the following analysis and experimentally-derived parameters.

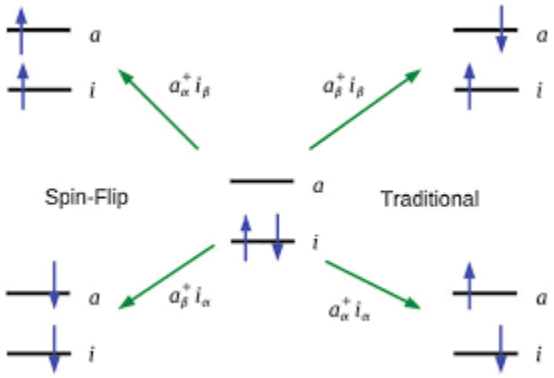


Figure 6: Spin flip scattering phenomena [19]

The probability of a spin flip process is modeled as P = [1 – exp (-δ)], where δ is the spin-flip parameter for interfaces.

For Nb/0.8 nm Fe/Nb, δ= 0.83+-0.08. [20] Hence, P = 0.56

Thus, taking into account spin-flip scattering in conjunction with the earlier processes, we deduce the critical current density of to be - $J_{c\,(Fe)} \sim 3.3 * 10^4$ A/cm$^2$

A similar analysis for Nb/3.8 nm Ni /Nb using a δ= 0.35+-0.05 [21] results in a P

= 0.29 and a critical current density of - $J_{c\,(Ni)} \sim 1.3 * 10^5$ A/cm$^2$

### 4.4 Conductivity calculations for hot spots

To verify our approach that quantifies the conductivity of each hot spot by the number of k-space points that satisfy the conservation conditions 2.1, 2.2 and 2.3 and the Andreev reflection conditions at the interface, we can the current results to the conductivity of each spot derived from conventional density of states analysis, using the parameters dE/dk, Fermi velocity, and the effective carrier mass.

The expressions for each of the parameters are as follows:

$$dE/dk = \frac{E_F\,(Nb) - E_F\,(Ni \text{ or } Fe)}{k_Z\,(Nb) - k_Z\,(Ni \text{ or } Fe)}$$

$$\text{Fermi velocity, } v_F\,(m/s) = \frac{1}{\hbar}\frac{dE}{dk}$$

$$\text{Effective Carrier mass, } (1/m^*)\,(kg) = \frac{1}{\hbar^2 k}\frac{dE}{dk}$$

$$\text{Conductivity, } \sigma\,(S/m) = \frac{ne^2 l}{m^* v_F}$$

The values of the dE/dk for iron and nickel are given below

| Hot spot no | Energy difference | dE/dk |
|---|---|---|
| Units | eV | (eVÅ) |
| 1 | 0.79 | 2.41 |
| 2 | 0.79 | 7.16 |
| 3 | 0.79 | 3.38 |
| 4 | 0.79 | 12.65 |

Table 4.3 List of space vectors for Nb/0.8 nm Fe/Nb, with dE/dk

| Hot spot no | Energy difference | dE/dk |
|---|---|---|
| Units | eV | (eVÅ) |
| 1 | 4.52 | 510.96 |
| 2 | 4.52 | 374.91 |
| 3 | 4.52 | 29.82 |
| 4 | 4.52 | 119.29 |
| 5 | 4.52 | 19.88 |
| 6 | 4.52 | 78.53 |
| 7 | 4.52 | 39.76 |
| 8 | 4.52 | 26.90 |
| 9 | 4.52 | 93.44 |

Table 4.4 List of space vectors for Nb/3.8 nm Ni /Nb, with dE/dk

Here $E_F$ is the Fermi energy, $k_Z$ is wave vector and ħ is reduced Planck's constant.

The values for Fermi velocity, effective carrier mass, and overall conductivity (sum of all conductivities of k-space vectors in a hot spot) are shown below. The mean free path was assumed to be 50 nm, which is greater than the coherence length of niobium (~40 nm)

| Hot spot number | Fermi velocity | Effective carrier mass of $e^-$ | Conductivity |
|---|---|---|---|
| | (m/s) | kg | (S/m) |
| 1 | 3.66E+05 | 9.44E-32 | 2.059E+08 |
| 2 | 1.09E+06 | 5.41E-31 | 6.114E+08 |
| 3 | 5.13E+05 | 4.82E-32 | 2.882E+08 |
| 4 | 1.92E+06 | 3.85E-32 | 1.081E+09 |

Table 4.5 Fermi velocity, effective carrier mass and conductivity of space vectors of Nb/0.8 nm Fe/Nb

| Hot spot number | Fermi velocity | Effective carrier mass of $e^-$ | Conductivity |
|---|---|---|---|
| | (m/s) | kg | (S/m) |
| 1 | 7.76E+07 | 2.32E-31 | 7.63E+09 |
| 2 | 5.70E+07 | 1.15E-31 | 5.60E+09 |
| 3 | 4.53E+06 | 3.53E-32 | 4.45E+08 |
| 4 | 1.81E+07 | 2.21E-33 | 1.78E+09 |
| 5 | 3.02E+06 | 7.94E-32 | 2.97E+08 |
| 6 | 1.19E+07 | 2.16E-31 | 1.17E+09 |
| 7 | 6.04E+06 | 1.98E-32 | 5.95E+08 |
| 8 | 4.09E+06 | 1.35E-31 | 4.01E+08 |
| 9 | 1.42E+07 | 1.10E-31 | 1.39E+09 |

Table 4.6 Fermi velocity, effective carrier mass and conductivity of space vectors of Nb/3.8 nm Ni /Nb

The conductivity % of each hotspot was then found out by dividing the value of conductivity of each hot spot by the total conductivity value.

| Hot Spot number | percentage conductivity of hot spot |
|---|---|
| | % |
| 1 | 9.42 |
| 2 | 27.98 |
| 3 | 13.19 |
| 4 | 49.47 |

Table 4.7 Conductivity and percentage of total conductivity for each hot spot Nb/0.8 nm Fe/Nb

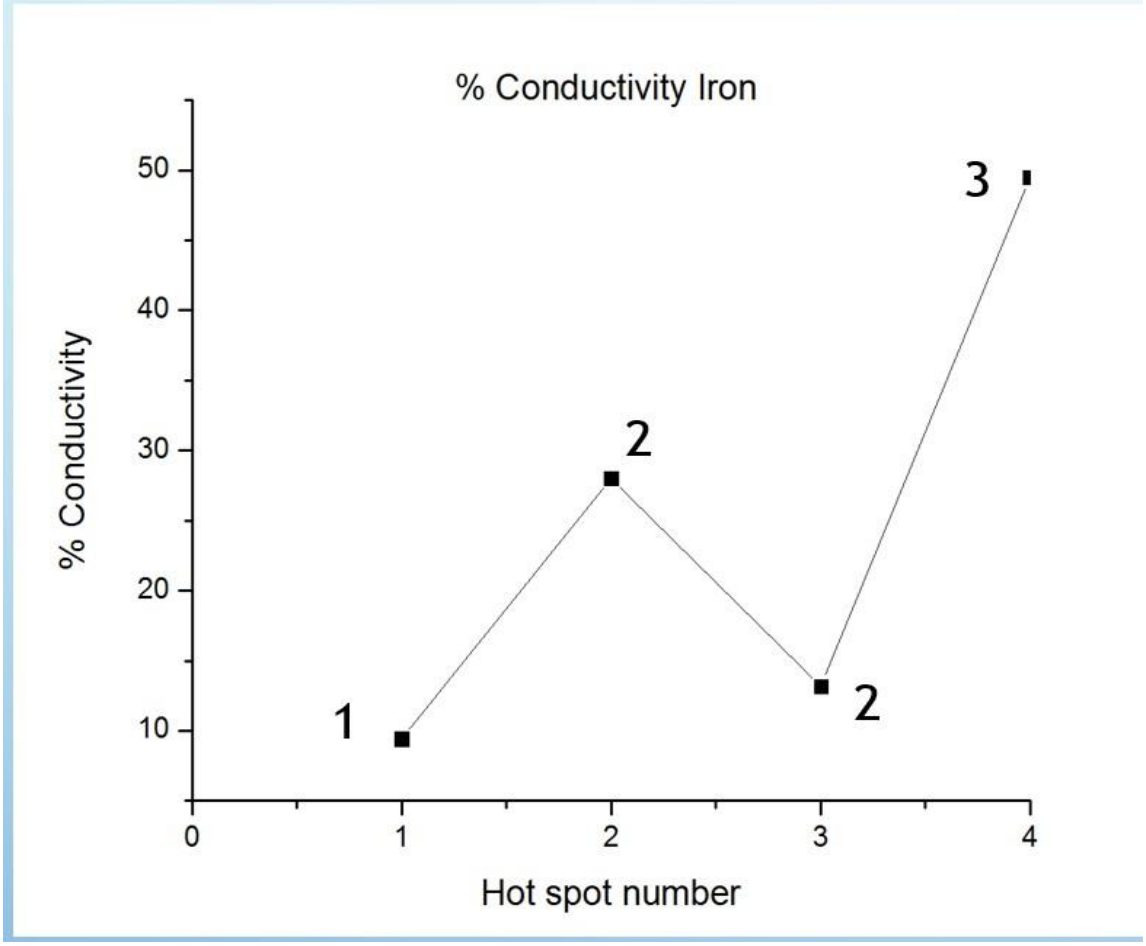


Figure 7: % Conductivity plot for Nb/0.8 nm Fe/Nb hot spots

In figure 18, the number near each value indicated the number of k-space vectors associated with each hot spot in Nb/0.8 nm Fe/Nb. From the % conductivity tables, we can clearly see that for iron, there is a conductivity % of 77.45 (close to 80%) through 2 hot spots out of the 4.

| Hot spot number | percentage conductivity of hot spot |
|---|---|
| | % |
| 1 | 39.52 |
| 2 | 28.99 |
| 3 | 2.31 |
| 4 | 9.23 |
| 5 | 1.54 |
| 6 | 6.07 |
| 7 | 3.08 |
| 8 | 2.08 |
| 9 | 7.23 |

Table 4.8 Conductivity and percentage of total conductivity for each hot spot Nb/3.8 nm Ni /Nb

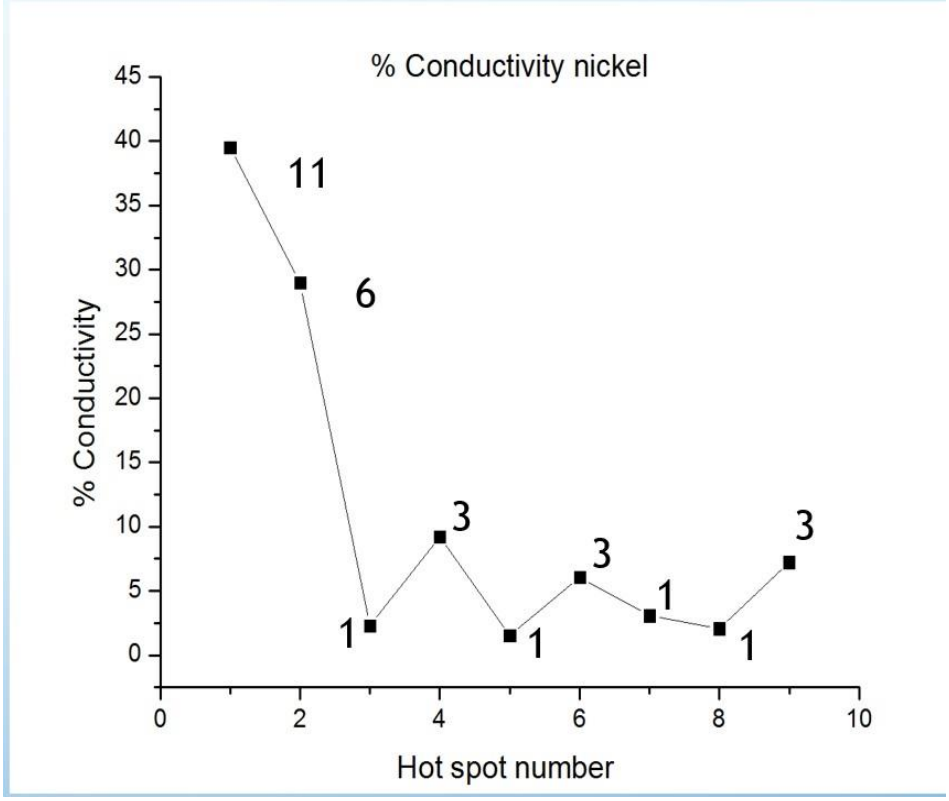


Figure 8: % Conductivity plot for Nb/3.8 nm Ni /Nb hot spots

In figure 19, the number near each value indicated the number of k-space vectors associated with each hot spot in Nb/3.8 nm Ni /Nb. Through nickel, there is a conductivity % of 68.51 (close to 70%) through 2 hot spots out of the 9.

**4.5 Qualitative corroboration of % conductivity using charge density plots**

The partial charge density for Nb/0.8 nm Fe/Nb and Nb/3.8 nm Ni /Nb was plotted for the bands near the Fermi level. This study was done to qualitatively corroborate the obtained % conductivity values obtained in the previous section.

Specific tags such as LPARD, IBAND, LSEPK and LSEPB are used to plot charge density at the energies near the Fermi level. Also, ICHARGE is set to 11.

The LPARD tag is used to evaluate partial densities. It must be set as .TRUE. The IBAND tag is used to specify the band number for which the charge density must be plotted. The LSEPK tag is used to save partial charge densities of different k-points in different files. The LSEPB tag is used to partial charge densities of different bands in different files.

The charge density for hot spot number 1 and 4 for Nb/0.8 nm Fe/Nb are plotted below.

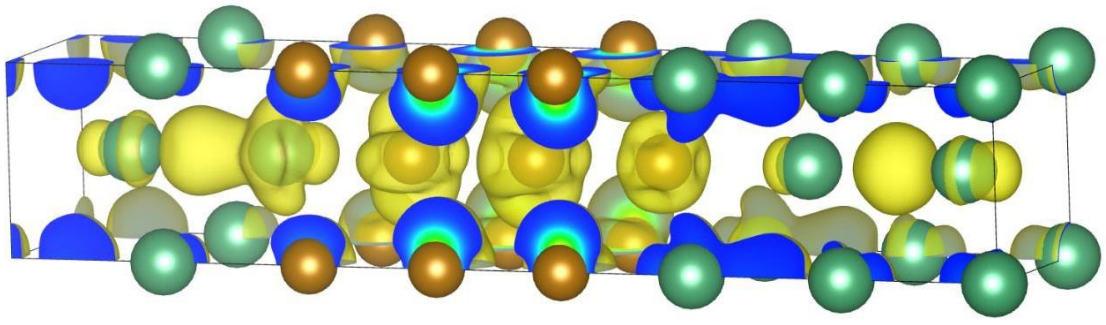

Figure 20: Charge density at hot spot 1 for Nb/0.8 nm Fe/Nb

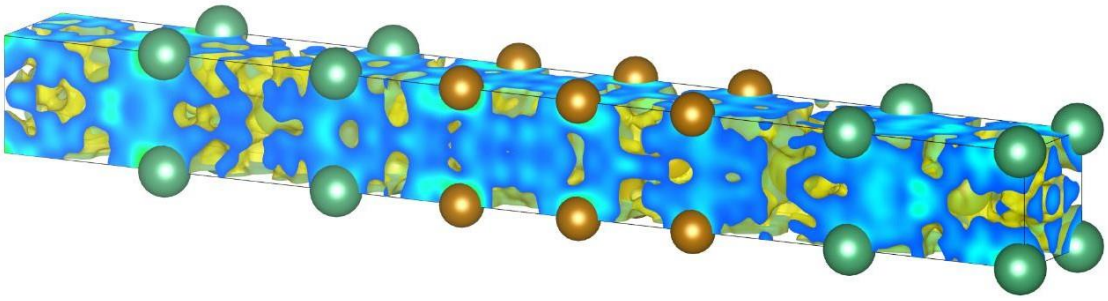

Figure 21: Charge density at hot spot 4 for Nb/0.8 nm Fe/Nb

The brown atoms are iron and the green atoms are niobium. From the above figures, it is pretty evident that the charge density values at hot spot 4 are more than that of the charge density values at hotspot 1. Isosurface value of 0.0005 was used consistently. This corraborates with the quantitative values obtained for conductivity and current density values for Nb/0.8 nm Fe/Nb.

The charge density for hot spot number 1 and 9 for Nb/3.8 nm Ni /Nb are plotted below.

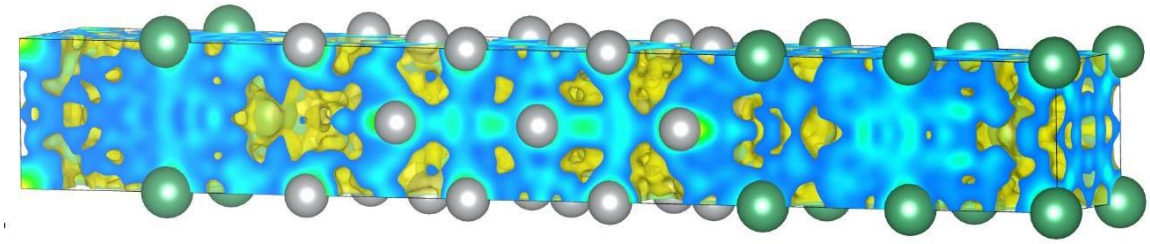

Figure 22: Charge density at hot spot 1 for Nb/3.8 nm Ni /Nb

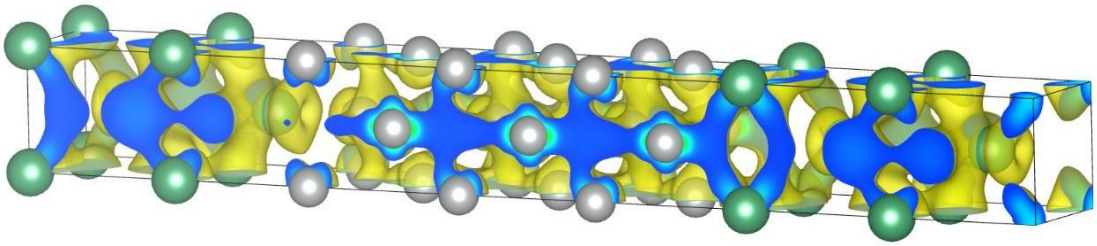

Figure 23: Charge density at hot spot 9 for Nb/3.8 nm Ni /Nb

The silver atoms are nickel and the green atoms are niobium. From the above figures, it is pretty evident that the charge density values at hot spot 1 are more than that of the charge density values at hotspot 9. Isosurface value of 0.0007 was used consistently. This corraborates with the quantitative values obtained for conductivity and current density values for Nb/3.8 nm Ni /Nb.

### 4.6 Transport through Ferromagnetic bulk

In the ferromagnetic bulk, the exchange splitting of majority and minority energy levels for each hotspot determines the rate of its wavefunction's decay and rotation as it progresses across the ferromagnetic bulk. We also have to take into account the spin-flip scattering in the ferromagnetic bulk.

The magnetic field also causes the evolution of the k-space vectors as it transverses through the ferromagnetic bulk. However, because of the short distance

traveled, order 5 nm, the change in k from the Lorentz force (qv X B) for Fe and Ni [with saturation fields of 0.14 T and 0.056 T, respectively] is insignificant (i.e. ~1 part in $10^3$ of the Brillion zone).

The critical currents analyzed at each of the hotspots are added to determine the net critical current. For iron-barrier junctions, the critical current density at the interface was found out to be 3.3 * $10^4$ A/cm$^2$ and for nickel barrier junctions, a critical current density of 1.3 * $10^5$ A/cm$^2$ was found at the interface.

| Hot Spot number | Fraction conductivity of hot spot | Current density |
|---|---|---|
| | | A/cm$^2$ |
| 1 | 0.094 | 3.1E+3 |
| 2 | 0.28 | 9.24E+3 |
| 3 | 0.13 | 4.29E+3 |
| 4 | 0.495 | 1.63E+4 |

Table 4.9Current density fraction of Nb/0.8 nm Fe/Nb hot spots

| Hot Spot number | Fraction conductivity of hot spot | Current density |
|---|---|---|
| | | A/cm$^2$ |
| 1 | 0.395 | 5.135E+4 |
| 2 | 0.290 | 3.77E+4 |
| 3 | 0.023 | 2.99E+3 |
| 4 | 0.092 | 1.196E+4 |
| 5 | 0.015 | 1.95E+3 |
| 6 | 0.061 | 7.93E+3 |
| 7 | 0.031 | 4.03E+3 |
| 8 | 0.021 | 2.73E+3 |
| 9 | 0.072 | 9.36E+3 |

Table 4.10 Current density fraction of Nb/3.8 nm Ni /Nb hot spots

A wavefunction decay equation is framed based on the two effects mentioned

above and the decay is calculated based on these two parameters.

Using equation 2.4, we can obtain the effect for exchange splitting field and using equations 2.5 and 2.6, we can obtain the effect of spin-flip scattering in the ferromagnetic bulk using values for x, β, $l_{sf}$ obtained from literature.

1. Decay due to the exchange splitting between majority and minority fields

   Once the pairs enter the ferromagnet, the pairs in each of the hot spots splits into a majority and minority band, based upon energy. This acts like a magnetic field, causing decay to the wavefunction of the pair of electrons. This is termed as an exchange splitting field. This exchange field is k-dependent.

   Below listed is the exchange splitting field effects for each hot spot. Each hot spot is evaluated separately since the exchange splitting field directly depends on the matched k-space vectors.

| Hot spot number | Exchange splitting field (eV) | Exchange splitting field effect | Current density ($A/cm^2$) |
|---|---|---|---|
| 1 | 1.86 | 0.70 | 2.17E+3 |
| 2 | 2.16 | 0.76 | 7.04E+3 |
| 3 | 2.28 | 0.78 | 3.35E+3 |
| 4 | 2.31 | 0.82 | 1.34E+4 |

Table 4.11 Exchange splitting field effect in Nb/0.8 nm Fe/Nb

| Hot spot number | Exchange splitting field (eV) | Exchange splitting field effect | Current density ($A/cm^2$) |
|---|---|---|---|
| 1 | 0.79 | 0.98 | 5.03E+4 |
| 2 | 0.67 | 0.99 | 3.73E+4 |
| 3 | 0.71 | 0.98 | 2.97E+3 |
| 4 | 0.77 | 0.99 | 1.195E+4 |
| 5 | 0.72 | 0.96 | 1.87E+3 |
| 6 | 0.67 | 0.97 | 7.7E+3 |
| 7 | 0.77 | 0.99 | 3.99E+3 |
| 8 | 0.76 | 0.76 | 2.09E+3 |
| 9 | 0.75 | 0.98 | 9.19E+3 |

Table 4.2 Exchange splitting field effect in Nb/3.8 nm Ni /Nb

2. Spin-flip scattering effect

The pairs of electrons also get affected by spin-flip scattering in the ferromagnetic bulk. The β value for iron was found to be 0.78 [22] and for nickel was found to be 0.14 [21] [23]

The $l_{sf}$ spin diffusion length was found to be 8.5 nm for iron and 21 nm for nickel. [13] The transport mean free path was calculated, and thereby the spin flip mean free path was calculated. The transport mean free path is directly dependent on the k-space vectors in a hot spot, and hence the values for each hot spot were evaluated. Note that for one of the hotspots, the values were very low, and this drove the Jc to 0.

| Hot Spot Number | Spin-flip scattering effect | Current density ($A/cm^2$) |
|---|---|---|
| 1 | 0.95 | 2.06E+03 |
| 2 | 0.94 | 6.61E+03 |
| 3 | 0.86 | 2.88E+03 |
| 4 | 0.75 | 1E+04 |

Table 4.13 Spin flip scattering effect in Nb/0.8 nm Fe/Nb

| Hot Spot Number | Spin-flip scattering effect | Current density ($A/cm^2$) |
|---|---|---|
| 1 | 0.91 | 4.58E+04 |
| 2 | 0.81 | 3.02E+04 |
| 3 | 0.81 | 2.41E+03 |
| 4 | - | - |
| 5 | 0.91 | 1.70E+03 |
| 6 | 0.87 | 6.70E+03 |
| 7 | 0.98 | 3.91E+03 |
| 8 | 0.97 | 2.03E+03 |
| 9 | 0.87 | 8.00E+03 |

Table 4.34 Spin flip scattering effect in Nb/3.8 nm Ni /Nb

The critical current density value for Nb/ 0.8nm Fe/Nb is - $J_{c\,(Fe)} \sim 2.18*10^4$ $A/cm^2$

The critical current density value for Nb/ 3.8nm Ni/Nb is - $J_{c\,(Ni)} \sim 1.01*10^5$ $A/cm^2$

**4.7 F/S interface**

Probability of $e^-$ flipping spin,

$P = [1 – \exp(-\delta)]$, where $\delta$ is the spin-flip parameter for interfaces

For Nb/0.8 nm Fe/Nb, $\delta = 0.83 \pm 0.08$. [20] Hence, $P = 0.56$

The critical current density value for Nb/ 0.8nm Fe/Nb is - $J_{c\,(Fe)} \sim 10^4$ $A/cm^2$

For Nb/3.8 nm Ni /Nb, $\delta = 0.35 \pm 0.05$. [21] Hence, $P = 0.29$

The critical current density value for Nb/ 3.8nm Ni/Nb is - $J_{c\,(Ni)} \sim 7.1*10^4$ $A/cm^2$

### 4.8 Final Results and comparison with experimental values

For the experimentally determined values of Jc versus thickness of the ferromagnetic layer, x, we will compare our results at the first maximum, which corresponds to a π-rotation of the wavefunction. At this thickness, the Jc is determined entirely by the drop in the wavefunction from the real part of k, and not by the oscillatory part from the imaginary part of k. Experimentally, the thickness of Fe to attain a π-rotation was determined to be 0.8 nm [24] and for nickel it is 3.8 nm [25].

The critical current density value for Nb/0.8 nm Fe/Nb was found to be $J_{c\ (Fe)} \sim 10^4$ A/cm$^2$. For Nb/0.8 nm Fe/Nb, the reported critical current density values vary from $8*10^3$ A/cm$^2$ to $3*10^4$ A/cm$^2$, depending on resistance values, and area of the junction. [26]. The critical current density value for Nb/3.8 nm Ni/Nb was found to be - $J_{c\ (Ni)} \sim 7.1 *10^4$ A/cm$^2$. For Nb/3.8 nm Ni/Nb, the reported critical current density values vary from $3*10^4$ A/cm$^2$ to $8*10^4$ A/cm$^2$, depending on resistance values, and area of the junction.[21][27]

## CHAPTER 5 CONCLUSIONS AND FUTURE WORK

It is evident that the use of the mean field exchange energy and empirical parameters for the interface and bulk material properties would not be expected to provide accurate predictions of the critical current density in JMRAM devices.

Through quantitative calculations of properties based on our realistic band parameter model, the results indicate that nearly 80% of current flows through 2 hot spots out of 4 of them in Nb/0.8 nm Fe/Nb structure, and nearly 70% current flows through 2 hot spots out of the 9 available in Nb/3.8 nm Ni /Nb. The charge density studies of Nb/0.8 nm Fe/Nb and Nb/3.8 nm Ni /Nb qualitatively corroborate with the obtained conductivities and critical current density values that were obtained for each hot spot.

Our model predicted the critical current density values to be:

Critical current density of Nb/0.8 nm Fe/Nb - $J_{c\,(Fe)} \sim 10^4$ A/cm$^2$

Critical current density of Nb/3.8 nm Ni/Nb - $J_{c\,(Ni)} \sim 7.1*10^4$ A/cm$^2$

These values are comparable to the reported experimental values for Nb/0.8 nm Fe/Nb, which lies between $8*10^3$ A/cm$^2$ to $3*10^4$ A/cm$^2$ and for Nb/3.8 nm Ni/Nb, which lies between $3*10^4$ A/cm$^2$ to $8*10^4$ A/cm$^2$.

The future work is to apply this model to further ferromagnetic materials like Cobalt, Gadolinium and alloys of Ni, Fe and Co. The results can be obtained through this model, by just feeding in the necessary values for those ferromagnetic elements and alloys. Hence, they can be relied upon when designing future JMRAM devices.

REFERENCES

[1] Gingrich, E. C., Bethany M. Niedzielski, Joseph A. Glick, Yixing Wang, D. L. Miller, Reza Loloee, W. P. Pratt Jr, and Norman O. Birge. "Controllable 0–π Josephson junctions containing a ferromagnetic spin valve." *Nature Physics* 12, no. 6 (2016): 564.

[2] Dayton, Ian M., Tessandra Sage, Eric C. Gingrich, Melissa G. Loving, Thomas F. Ambrose, Nathan P. Siwak, Shawn Keebaugh et al. "Experimental Demonstration of a Josephson Magnetic Memory Cell With a Programmable $\pi $-Junction." *IEEE Magnetics Letters* 9 (2018): 1-5.

[3] Bruce F. Cockburn, 2004 International Workshop on Memory Technology, Design and Testing (MTDT'04)

[4] Bell, C., G. Burnell, C. W. Leung, E. J. Tarte, D-J. Kang, and M. G. Blamire. "Controllable Josephson current through a pseudospin-valve structure." *Applied physics letters* 84, no. 7 (2004): 1153-1155.

[5] Herr, Quentin P., Andrew D. Smith, and Michael S. Wire. "High speed data link between digital superconductor chips." *Applied physics letters* 80, no. 17 (2002): 3210-3212.

[6] Kawahara, Takayuki, Kenchi Ito, Riichiro Takemura, and Hideo Ohno. "Spin-transfer torque RAM technology: Review and prospect." *Microelectronics Reliability* 52, no. 4 (2012): 613-627.

[7] El Qader, M.A., 2016. Proximity in Hybrid Superconductor/Ferromagnetic Structures (Doctoral dissertation, Arizona State University).

[8] Kontos, T., M. Aprili, J. Lesueur, X. Grison, and L. Dumoulin. "Superconducting proximity effect at the paramagnetic-ferromagnetic transition." *Physical review letters* 93, no. 13 (2004): 137001.

[9] Cuevas, Juan Carlos. "Introduction to density functional theory." *Universität Karlsruhe, Germany* (2010)..

[10] E. A. Demler, G. B. Arnold* and M. R. Beasley, 1997. Superconducting proximity effects in magnetic metals. *Physical review B*, 55, No 22

[11] Abd El Qader, Makram, R. K. Singh, Sarah N. Galvin, L. Yu, J. M. Rowell, and N. Newman. "Switching at small magnetic fields in Josephson junctions fabricated with ferromagnetic barrier layers." *Applied Physics Letters* 104, no. 2 (2014): 022602.

[12] Buzdin, Alexandre I. "Proximity effects in superconductor-ferromagnet heterostructures." *Reviews of modern physics* 77, no. 3 (2005): 935.

[13] Jack Bass and William P. Pratt Jr, 2007. Spin-Diffusion Lengths in Metals and Alloys, and Spin-Flipping at Metal/Metal Interfaces: an Experimentalist's Critical Review.

[14] Schäfer, Jörg, M. Hoinkis, Eli Rotenberg, Peter Blaha, and R. Claessen. "Fermi surface and electron correlation effects of ferromagnetic iron." *Physical Review B* 72, no. 15 (2005): 155115.

[15] Kalyana Raman, Dheepak Surya. "The VASP Manual" https://cms.mpi.univie.ac.at/wiki/index.php/The_VASP_Manual

[16] Momma, Koichi, and Fujio Izumi. "VESTA: a three-dimensional visualization system for electronic and structural analysis." *Journal of Applied Crystallography* 41, no. 3 (2008): 653-658.

[17] Kalyana Raman Dheepak Surya http://materialsproject.org/

[18] Luo, Pengshun S., Thierry Crozes, Bruno Gilles, Sukumar Rajauria, Bernard Pannetier, and Hervé Courtois. "Spin-valve effect of spin-accumulation resistance in a double ferromagnet/superconductor junction." *Physical Review B* 79, no. 14 (2009): 140508.

[19] Sandweg, Christian W., Yosuke Kajiwara, Andrii V. Chumak, Alexander A. Serga, Vitaliy I. Vasyuchka, Mattias Benjamin Jungfleisch, Eiji Saitoh, and Burkard Hillebrands. "Spin pumping by parametrically excited exchange magnons." *Physical review letters* 106, no. 21 (2011): 216601.

[20] A. Sharma, J. A. Romero, N. Theodoropoulou, R. Loloee, W. P. Pratt, and J. Bass, 2007.Specific resistance and scattering asymmetry of Py/Pd, Fe/V, Fe/Nb, and Co/Pt interfaces. *Journal of Applied Physics 102*, p.113916.

[21] Nguyen, H. Y. T., R. Acharyya, E. Huey, B. Richard, R. Loloee, W. P. Pratt Jr, J. Bass, Shuai Wang, and Ke Xia. "Conduction electron scattering and spin flipping at sputtered Co/Ni interfaces." *Physical Review B* 82, no. 22 (2010): 220401.

[22] Theodoropoulou, N., A. Sharma, T. Haillard, R. Loloee, W. P. Pratt, J. Bass, J. Zhang, and M. A. Crimp. "Specific Resistance, Scattering Asymmetry, and Some Thermal Instability, of Co/Al, Fe/Al, and $Co_{91}Fe_9$/Al Interfaces." *IEEE transactions on magnetics* 43, no. 6 (2007): 2860-2862.

[23] Moreau, Charles E., Ion C. Moraru, Norman O. Birge, and William P. Pratt Jr. "Measurement of spin diffusion length in sputtered Ni films using a special exchange-biased spin valve geometry." *Applied physics letters* 90, no. 1 (2007): 012101.

[24] Th. Mühge, N. N. Garif'yanov, Yu. V. Goryunov, G. G. Khaliullin, L. R. Tagirov,

K. Westerholt, I. A. Garifullin, and H. Zabel, 1996. Possible Origin for Oscillatory Superconducting Transition Temperature in Superconductor/Ferromagnet Multilayers. *Physical Review Letters 77*, No 9 (1996): 1857

[25] Robinson, J. W. A., S. Piano, G. Burnell, C. Bell, and M. G. Blamire. "Critical current oscillations in strong ferromagnetic π junctions." *Physical review letters* 97, no. 17 (2006): 177003.

[26] Robinson, J. W. A., S. Piano, G. Burnell, C. Bell, and M. G. Blamire. "Zero to π transition in superconductor-ferromagnet-superconductor junctions." *Physical Review B* 76, no. 9 (2007): 094522.

[27] Blum, Y., A. Tsukernik, M. Karpovski, and A. Palevski. "Oscillations of the superconducting critical current in Nb-Cu-Ni-Cu-Nb junctions." *Phyical review letters* 89, no.18 (2002): 187004.